Transport and Communications Science Journal, Vol. 77, Issue 09 (11/2026), 1275-1290

Transport and Communications Science Journal

CFD-BASED INVESTIGATION OF TEMPORAL CLEAR-WATER LOCAL SCOUR AROUND A CYLINDRICAL BRIDGE PIER USING REEF3D

Mai Quang Huy*, Nguyen Dang Phong

University of Transport and Communications, No 3 Cau Giay Street, Hanoi, Vietnam

ARTICLE INFO

TYPE: Research Article
Received: 16/08/2026
Revised: 06/11/2026
Accepted: 11/11/2026
Published online: 15/11/2026
https://doi.org/10.47869/tcsj.77.9.11

* *Corresponding author*
Email: mqhuy@utc.edu.vn; Tel: +84 987899335

Abstract. Local scour around bridge piers is a major threat to foundation stability, and accurate prediction of its temporal development is important for bridge safety assessment. This study investigates clear-water local scour around a cylindrical bridge pier using an existing laboratory dataset and three-dimensional CFD-based morphodynamic simulation with REEF3D. The experimental dataset comprises 21 time-resolved scour-depth measurements collected over a 330-min test. The numerical model solves the incompressible RANS equations with the standard k-ω turbulence model and couples the hydrodynamic solution with the Engelund–Fredsøe bed-load formulation and movable-bed evolution. Mesh-resolution and critical Shields parameter sensitivity analyses were conducted to identify a suitable calibrated configuration. The selected configuration reproduced the measured temporal scour development with satisfactory agreement and captured the characteristic progression from rapid initial erosion through transitional scour growth to gradual stabilization toward quasi-equilibrium. The results indicate that a properly calibrated REEF3D framework can reproduce the temporal development of clear-water pier scour with reasonable accuracy, although broader independent validation is required before general engineering application.

Keywords: bridge pier scour, clear-water scour, CFD, morphodynamic modeling, REEF3D, sediment transport.

@ 2026 University of Transport and Communications

1. INTRODUCTION

Bridges are essential transportation assets, yet hydraulic failures remain one of the most persistent threats to their structural safety. Historical investigations have repeatedly identified flooding and scour among the principal causes of bridge damage and collapse worldwide [1-4]. In particular, scour-induced loss of foundation support can substantially reduce structural stability and may lead to sudden failure during extreme flood events [3]. A recent large-scale review of historical bridge collapses identified hydraulic actions as one of the five leading causes of bridge failure worldwide, together with design errors, construction defects, collision, and overload [5]. Improving the reliability of scour prediction at bridge foundations therefore remains an important challenge in bridge safety assessment.

Among the different mechanisms affecting bridge foundations, local scour around bridge piers is particularly difficult to predict because it is governed by highly three-dimensional flow–sediment interactions. As the approaching flow encounters the pier, a stagnation zone develops at the upstream face, generating a downward flow that impinges on the bed and initiates the horseshoe vortex system, which is widely recognized as a dominant mechanism driving sediment entrainment near the pier base [6, 7]. The principal hydrodynamic mechanisms responsible for local scour development are conceptually illustrated in Fig. 1. In addition to the horseshoe vortex system, flow acceleration around the pier sides and vortex shedding in the downstream wake further intensify local bed shear stresses, resulting in a highly nonlinear scour process influenced by hydraulic conditions, sediment characteristics, pier geometry, and flow regime.

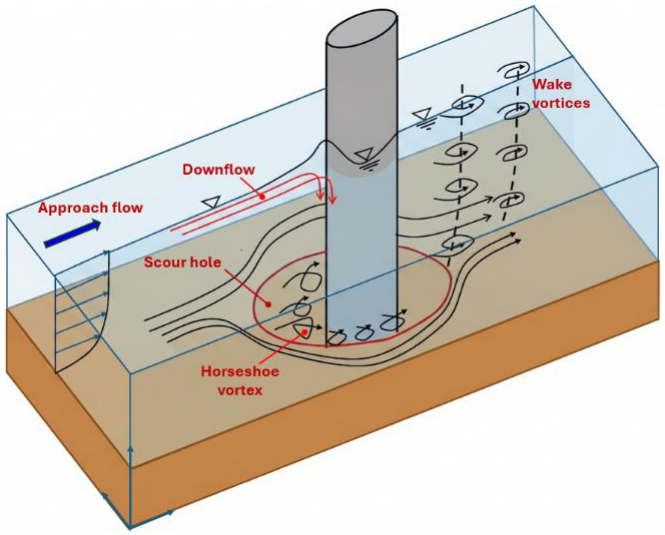


Figure 1. Conceptual illustration of three-dimensional flow structures and local scour mechanisms around a cylindrical bridge pier under clear-water conditions.

Because of the engineering importance of bridge pier scour, numerous empirical and semi-empirical prediction methods have been developed over the past decades. Widely used empirical approaches include those proposed by Breusers et al. [8], Froehlich [9], Melville and Coleman [6], and the HEC-18 methodology [10], owing to their simplicity and ease of application in bridge design. However, these methods are inherently constrained by the experimental conditions under which they were developed and may exhibit substantial variability when applied outside their calibration ranges. Recent comparative studies have also demonstrated that scour predictions can be highly sensitive to hydraulic, sediment, and

geometric conditions, as well as to the specific empirical formulation adopted [11]. Their simplified representation of the governing hydrodynamic mechanisms further limits their ability to reproduce the detailed transient processes associated with scour initiation, growth, and equilibrium development.

Physical laboratory experiments have significantly advanced the understanding of local scour processes by providing controlled observations of the influence of hydraulic intensity, sediment characteristics, and pier geometry on scour development. Previous experimental studies have clarified important mechanisms governing local scour formation and provided valuable datasets for engineering model development [12]. Nevertheless, laboratory investigations remain time-consuming, expensive, and often limited in their ability to capture detailed spatial and temporal flow–sediment interactions at high resolution.

Advances in computational fluid dynamics (CFD) have created new opportunities for investigating bridge-scour processes with greater physical realism. Unlike empirical methods, CFD-based approaches can resolve the three-dimensional hydrodynamic field and provide spatially distributed information on velocity, turbulence, pressure, and bed shear stress [7, 13]. When coupled with sediment-transport and morphodynamic formulations, such models can additionally simulate the temporal evolution of scour and the associated bed deformation [14-16]. Earlier numerical studies demonstrated the feasibility of three-dimensional bridge-pier scour simulation [7, 17] while subsequent developments introduced coupled hydrodynamic–morphodynamic frameworks capable of reproducing transient scour development and evolving bed morphology [13]. However, numerical predictions remain sensitive to turbulence closure, grid resolution, and other model settings, and recent numerical studies have emphasized the importance of verifying turbulence models and mesh sizes against experimental observations [13, 18, 20]. Consequently, careful calibration and comparison with laboratory or field measurements remain essential before CFD-based scour models can be applied confidently in engineering practice.

Among available CFD platforms, the open-source framework REEF3D has emerged as a promising tool for free-surface hydrodynamics, sediment transport, and morphodynamic simulation [21, 22]. Previous studies have demonstrated its successful application to erosion and scour-related hydraulic problems, including sediment erosion near hydraulic structures, pier scour under combined wave and current conditions [23], and scour processes around submerged structural components [24]. These studies indicate the considerable potential of REEF3D for scour simulation. However, relatively limited research has systematically evaluated the capability of REEF3D to reproduce clear-water local scour around bridge piers under controlled fluvial laboratory conditions, particularly with detailed validation against transient experimental measurements.

A common limitation of CFD-based scour studies is that validation often focuses on the final equilibrium depth, with less attention to the temporal development of scour. In this study, REEF3D is evaluated against a laboratory dataset containing 21 time-resolved scour-depth measurements collected over a 330-min clear-water test around a cylindrical pier. Mesh resolution and the critical Shields parameter are examined to identify a calibrated numerical configuration, which is subsequently evaluated using the measured scour-development curve, MAE, RMSE, and final scour depth. The contribution of this study lies in combining a 21-point laboratory scour time series with systematic mesh and sediment-threshold sensitivity analyses to assess the ability of REEF3D to reproduce the full transient development of clear-water scour around a cylindrical pier. Clear-water conditions were considered to isolate pier-induced local

sediment entrainment from upstream sediment supply, while the cylindrical pier provides a standard benchmark geometry without flow-orientation effects. The results provide a case-specific assessment of the strengths and limitations of REEF3D for temporal prediction of clear-water pier scour.

2. METHODOLOGY

2.1. Experimental dataset

The numerical simulations were assessed against a laboratory dataset obtained from controlled clear-water scour experiments around a cylindrical bridge pier. The original experiments were conducted by Nguyen Dang Phong [25], and the experimental data were made available for the present study through direct collaboration with the experimental investigator. The principal experimental conditions are summarized in Table 1, and the experimental configuration is shown in Fig. 2.

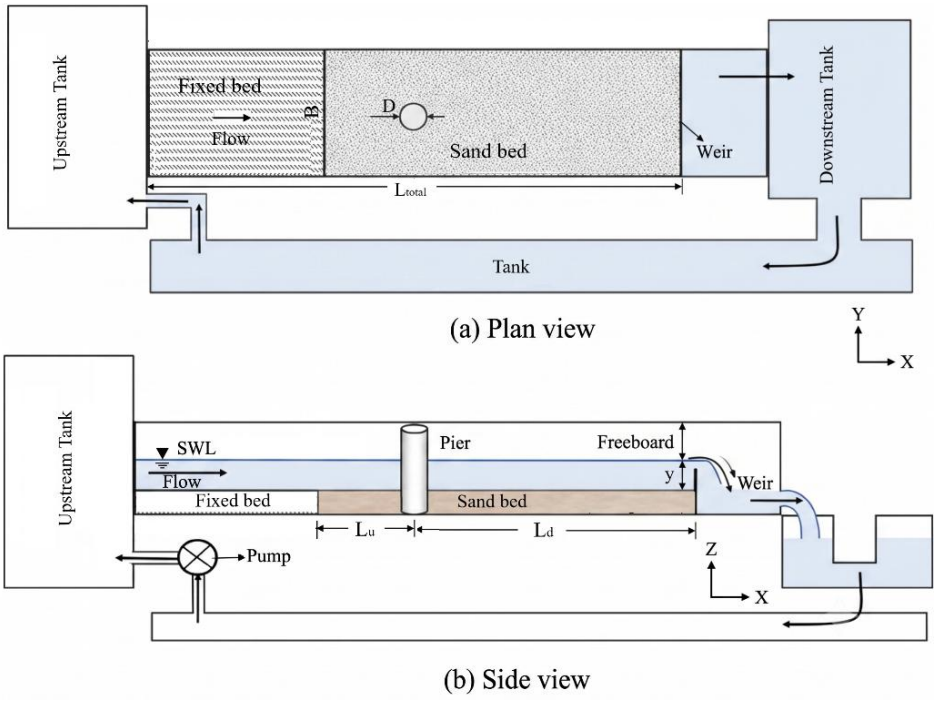


Figure 2. Schematic diagram of the experimental setup: (a) plan view and (b) side view.

The experiments were conducted in a recirculating flume approximately 20.0 m long, 1.0 m wide, and 0.75 m deep. The movable-bed section was 8.0 m long and contained a 0.25 m-thick layer of nearly uniform non-cohesive sand. A cylindrical pier with a diameter of $D = 0.07$ m was installed along the flume centerline, with its center located 3.5 m downstream from the upstream end of the movable-bed section.

The sediment had a median grain diameter of $d_{50} = 0.27$ mm, a density of 2,650 kg/m^3, a bed porosity of 0.45, a geometric standard deviation of 1.3, and an angle of repose of 35^o. A constant discharge of $Q = 0.040$ m^3/s produced an approach velocity of $U = 0.222$ m/s and a flow depth of 0.18 m. The critical approach velocity for sediment motion was estimated following Liang et al. [26], in which the critical mean velocity is expressed as $U_c = 5.75u_{*c}\log_{10}(5.53h/d_{50})$, where u_{*c} is the critical shear velocity determined from the Shields diagram. Using $d_{50} = 0.27$ mm and $h = 0.18$ m gives $U_c = 0.277$ m/s and $U/U_c = 0.80<1$, confirming the clear-water scour condition.

The experiment was conducted for 330 min (5.5 h). The maximum scour depth was measured at 21 time intervals, providing a time-resolved dataset ds(t) for evaluating scour initiation, development, and gradual stabilization. The measured maximum scour depth at the end of the experiment was approximately 54.0 mm.

Table 1. Experimental hydraulic, geometric, sediment, and observation parameters used for model calibration and performance assessment.

Category	Parameter	Symbol	Value	Unit
Hydraulic conditions	Discharge	Q	0.040	m³/s
	Approach flow velocity	U	0.222	m/s
	Critical velocity	U_c	0.277	m/s
	Flow intensity	U/U_c	0.80	
	Flow depth	y	0.18	m
	Water temperature	T	20	°C
Geometric configuration	Total flume length	L_{total}	20.0	m
	Movable sediment section length	L_s	8.0	m
	Flume width	B	1.0	m
	Flume height	H	0.75	m
	Cylindrical pier diameter	D	0.07	m
	Distance from movable bed inlet to pier center	L_u	3.5	m
	Distance from pier center to movable bed outlet	L_d	4.5	m
Sediment properties	Median grain diameter	d_{50}	0.27	mm
	Sediment density	ρ_s	2650	kg/m³
	Bed porosity	n	0.45	–
	Geometric gradation coefficient	σ_g	1.3	–
	Angle of repose	ϕ	35	°
	Sediment bed thickness	h_s	0.25	m
Experimental observations	Final measured maximum scour depth	$d_{s,max}$	0.054	m
	Experimental duration	t_{exp}	330	min
	Number of temporal scour measurements	–	21	–

2.2. Governing equations

The hydrodynamic flow field was simulated using the three-dimensional incompressible Reynolds-averaged Navier–Stokes (RANS) equations, which describe conservation of mass and momentum for turbulent free-surface flow [21,22].

- The continuity equation is given by:

$$\frac{\partial \mathrm{u}_i}{\partial \mathrm{x}_i} = 0 \tag{1}$$

where u_i denotes the velocity components in Cartesian coordinates.

- The momentum conservation equations are expressed as:

$$\frac{\partial u_i}{\partial t} + u_j \frac{\partial u_i}{\partial x_j} = -\frac{1}{\rho}\frac{\partial p}{\partial x_i} + \frac{\partial}{\partial x_j}\left[\nu\left(\frac{\partial u_i}{\partial x_j} + \frac{\partial u_j}{\partial x_i}\right) - \overline{u_i' u_j'}\right] + g_i \tag{2}$$

where t is time, ρ is the fluid density, p is the pressure, ν is the kinematic viscosity, g_i represents gravitational acceleration, and $-\overline{u_i' u_j'}$ denotes the Reynolds stress tensor associated with turbulent fluctuations.

Because local scour around bridge piers is governed by highly three-dimensional hydrodynamic processes involving flow separation, downflow formation, vortex generation, and evolving sediment interaction, a fully three-dimensional numerical framework was considered necessary.

The governing equations were solved using the open-source CFD framework REEF3D, which has been developed for three-dimensional free-surface hydrodynamics, sediment transport, and morphodynamic simulations [21, 22]. Previous studies have demonstrated its application to scour-related hydraulic problems, including pier scour under current and wave conditions [23] and local scour around submerged bridge decks [24].

2.3. Turbulence closure and numerical framework

Turbulence was represented using the standard $k-\omega$ RANS model implemented in REEF3D. The Reynolds stresses were closed using the Boussinesq approximation [18, 19, 27]:

$$-\overline{u_i' u_j'} = \nu_t \left(\frac{\partial u_i}{\partial x_j} + \frac{\partial u_j}{\partial x_i} \right) - \frac{2}{3} k \delta_{ij}, \tag{3}$$

where k is the turbulent kinetic energy, ν_t is the turbulent eddy viscosity, and δ_{ij} is the Kronecker delta. The eddy viscosity is defined as

$$\nu_t = c_\mu \frac{k}{\omega},$$

where ω is the specific turbulent dissipation rate. The transport equations for k and ω are written as [22]

$$\frac{\partial k}{\partial t} + u_j \frac{\partial k}{\partial x_j} = \frac{\partial}{\partial x_j} \left[\left(\nu + \frac{\nu_t}{\sigma_k} \right) \frac{\partial k}{\partial x_j} \right] + P_k - \beta_k k \omega, \tag{4}$$

and

$$\frac{\partial \omega}{\partial t} + u_j \frac{\partial \omega}{\partial x_j} = \frac{\partial}{\partial x_j} \left[\left(\nu + \frac{\nu_t}{\sigma_\omega} \right) \frac{\partial \omega}{\partial x_j} \right] + \frac{\omega}{k} \alpha P_k - \beta \omega^2 , \tag{5}$$

where P_k is the turbulent production rate, and α, β_k, β,σ_k, and σ_ω are model coefficients. In REEF3D, the standard coefficients are $\alpha = 5/9$, $\beta_k = 9/100$, $\beta = 3/40$, and $\sigma_k = \sigma_\omega = 2$ [22]. Near solid boundaries, wall effects and surface roughness were treated using the Schlichting rough-wall law implemented in REEF3D.

The free surface was captured using the level-set method, while the cylindrical pier was represented using the immersed boundary method (IBM) within a Cartesian grid. Spatial discretization employed a high-order weighted essentially non-oscillatory (WENO) scheme, temporal integration was performed using a third-order Runge–Kutta method, and pressure–velocity coupling was handled using a projection method [21, 22].

2.4. Sediment transport and bed evolution

To simulate local scour development around the bridge pier, the hydrodynamic solver was coupled with a morphodynamic sediment transport framework within REEF3D. Sediment transport was modeled using the Engelund–Fredsøe formulation [28], which has been widely applied for non-cohesive sediment transport under open-channel flow conditions and has demonstrated suitability for scour-related hydraulic simulations.

The evolution of the movable bed was governed by the sediment continuity (Exner) equation [29]:

$$(1-n)\frac{\partial z_b}{\partial t}+\frac{\partial q_{bx}}{\partial x}+\frac{\partial q_{by}}{\partial y}=0 \tag{6}$$

where n is the bed porosity, z_b is the bed elevation, and q_{bx} and q_{by} are the volumetric bed-load transport rates in the streamwise and transverse directions, respectively.

Sediment entrainment was controlled through the critical Shields parameter θ_c, which defines the threshold for incipient particle motion. Since the selection of this parameter can significantly influence predicted scour rates and final bed morphology, a sensitivity analysis was conducted using three representative values θ_c = 0.04, 0.042, 0.047. These values were selected to reflect the range commonly adopted in sediment transport applications for uniform non-cohesive sand under comparable hydraulic conditions [21, 22].

The angle of repose of the sediment was specified as 35°, consistent with the experimental sediment characteristics, in order to ensure physically realistic slope stabilization during bed evolution. This parameter is particularly important in localized scour simulations, where steep bed slopes may develop around the pier as erosion progresses.

Because hydrodynamic and morphodynamic processes evolve over different characteristic time scales, REEF3D employs a fully decoupled time-step approach [22] in which the hydrodynamic and sediment-transport calculations are advanced independently. The morphodynamic time step, t_{sed}, is generally larger than the hydrodynamic time step, t_{hyd}, and is related through a relaxation factor, *rel*, as

$$t_{sed}=\frac{t_{hyd}}{rel} \tag{7}$$

A time-step ratio t_{sed}/t_{hyd} = 500 was used in all simulations, corresponding to *rel* = 0.002.

2.5. Computational setup

The computational domain reproduced the 8.0 m movable-bed section of the laboratory flume, including the cylindrical pier, flow depth, sediment-bed thickness, and channel width. The pier was positioned along the flume centreline, 3.5 m downstream from the upstream boundary of the movable bed.

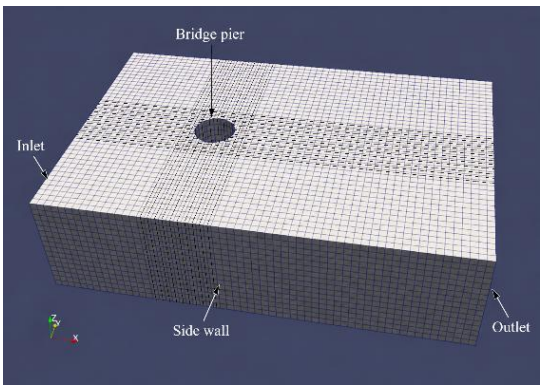


Figure 3. Representative Cartesian computational mesh used in the REEF3D simulations.

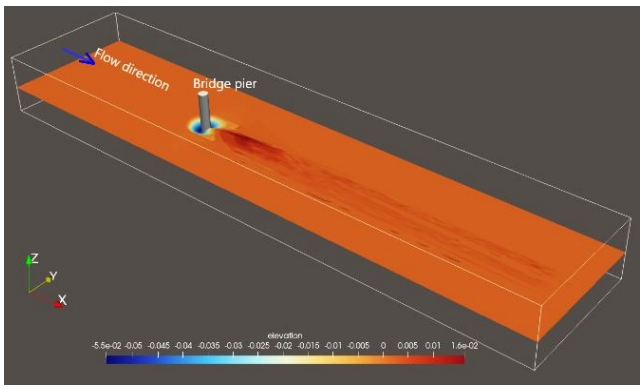


Figure 4. Representative three-dimensional bed-elevation result obtained from the present REEF3D simulation.

The computational domain was selected to reproduce the full movable-bed reach of the laboratory flume rather than a truncated near-pier subdomain. Relative to the pier diameter, the upstream and downstream distances were (L_u/D = 50) and (L_d/D = 64.3), respectively, while the channel-width ratio was (B/D = 14.3). The lateral clearance between the pier surface and each sidewall was approximately (6.64D), and the pier-to-channel-width blockage ratio was 7%. These dimensions provide substantial upstream, downstream, and lateral distances around the pier and were retained to minimize artificial boundary interference while maintaining consistency with the physical flume configuration.

A uniform streamwise velocity was prescribed at the inlet. A zero-gradient condition was applied at the downstream boundary, while the upper boundary was treated as an atmospheric free surface. The flume sidewalls and pier surface were specified as no-slip boundaries, and the channel bed was defined as a movable sediment boundary. The hydraulic and sediment properties were assigned according to the experimental values summarized in Table 1.

To examine the influence of spatial resolution, three Cartesian mesh configurations were considered, with characteristic cell sizes near the pier of 7, 5, and 4 mm. The corresponding meshes are referred to as the coarse, medium, and fine cases, respectively. A representative view of the computational mesh is shown in Fig. 3.

Each numerical simulation covered the full experimental duration of 330 min (5.5 h). To reduce computational cost associated with long-duration morphodynamic calculations, the simulations employed the time-step decoupling strategy described in Section 2.4. The computations were performed on a workstation equipped with an Intel Xeon E5-2680R v4 processor (14 cores, 28 threads), 64 GB RAM, and an NVIDIA Quadro M4000 graphics card.

To illustrate the three-dimensional morphodynamic output available from REEF3D, Fig. 4 presents a representative visualization of the simulated movable-bed deformation around the cylindrical pier. This figure is included to demonstrate the model-output capability rather than for quantitative validation of equilibrium scour morphology.

2.6. Model calibration and performance assessment

Model calibration and performance assessment were conducted using the experimental dataset described in Section 2.1. A major advantage of the available dataset is that it supports model performance assessment not only against the final scour depth, but also against the full temporal evolution of scour depth development.

The primary assessment variable was the time-dependent scour depth $d_s(t)$, measured at 21 observation points over the 330-minute experimental duration. This dataset enables assessment of the model's capability to reproduce both the transient development of local scour and the asymptotic approach toward equilibrium conditions. The predictive accuracy of the numerical simulations was quantified using standard statistical error metrics, including the mean absolute error (*MAE*), root mean square error (*RMSE*), and relative error in final scour depth.

The *MAE* was calculated as:

$$MAE = \frac{1}{N}\sum_{i=1}^{N} | d_{s,i}^{sim} - d_{s,i}^{exp} | \tag{8}$$

The *RMSE* was defined as:

$$\mathrm{RMSE} = \sqrt{\frac{1}{N}\sum_{i=1}^{N}(d_{s,i}^{sim} - d_{s,i}^{exp})^2} \tag{9}$$

The relative final scour error ε was calculated as:

$$\varepsilon = \frac{|\, d_{s,eq}^{sim} - d_{s,eq}^{exp} \,|}{d_{s,eq}^{exp}} \times 100\% \tag{10}$$

where: $d_{s,i}^{sim}$= simulated scour depth; $d_{s,i}^{exp}$= measured scour depth; $d_{s,eq}^{sim}$= simulated final scour depth; $d_{s,eq}^{exp}$= measured final scour depth; N= number of temporal measurements

Because the mesh resolution and critical Shields parameter were selected using the same experimental dataset, the resulting comparison is interpreted as a calibrated model assessment rather than fully independent validation. The emphasis of the present study is therefore on the ability of REEF3D to reproduce the measured temporal development of clear-water pier scour.

3. RESULTS AND DISCUSSION

3.1. Mesh-sensitivity analysis

A mesh-sensitivity analysis was performed to evaluate the influence of spatial resolution on the predicted maximum scour depth. Three Cartesian mesh configurations were considered, with characteristic cell sizes near the pier of 7, 5, and 4 mm, corresponding to the coarse, medium, and fine meshes, respectively. All other hydraulic, sediment, and numerical settings were kept unchanged. The critical Shields parameter was fixed at θ_c = 0.042 for all mesh cases The principal results are summarized in Table 2.

Table 2. Mesh-sensitivity analysis for scour-depth prediction.

Mesh	Δx (mm)	Cells ($\times 10^6$)	Predicted scour depth d_s (mm)	Absolute relative error ε (%)	CPU time (h)
Coarse	7.0	1.12	44.90	16.85	26
Medium	5.0	2.16	56.31	4.28	62
Fine	4.0	3.85	55.94	3.59	138

The coarse mesh substantially underestimated the measured scour depth of 54.0 mm, with ε = 16.85%. Refinement to the medium mesh markedly improved the prediction, yielding $d_{s\max}$ = 56.31mm and ε = 4.28%. Further refinement to the fine mesh produced only a small change in the predicted scour depth, from 56.31 to 55.94 mm, while increasing the total number of computational cells from approximately 2.16 to 3.85 million.

Although the fine mesh gave a slightly smaller relative error, the improvement over the medium mesh was marginal compared with the additional computational demand. The medium mesh was therefore selected as a practical compromise between predictive accuracy and computational efficiency and was used in the subsequent sensitivity and temporal scour simulations.

3.2. Sensitivity to the critical Shields parameter

The critical Shields parameter, θ_c, defines the threshold for sediment entrainment and therefore directly influences the predicted scour response. To evaluate its sensitivity, three values were examined θ_c = 0.040, 0.042, and 0.047. All simulations were performed using the medium mesh configuration, while the remaining hydraulic, sediment, and numerical parameters were kept unchanged. The results are summarized in Table 3.

The predicted scour depth decreased systematically with increasing θ_c. At θ_c = 0.040, the lower entrainment threshold increased sediment mobility and produced a scour depth of 59.44 mm, corresponding to ε = 10.07%. Increasing θ_c to 0.047 reduced sediment mobility and resulted in a scour depth of 48.20 mm, with ε = 10.74%.

Table 3. Sensitivity of predicted scour depth to the critical Shields parameter.

Case	θ_c	Predicted scour depth d_s (mm)	*Error* ε (%)	Interpretation
1	0.040	59.44	10.07	Overprediction
2	0.042	56.31	4.28	Best agreement
3	0.047	48.20	10.74	Underprediction

Among the tested values, θ_c = 0.042 provided the closest agreement with the measured scour depth, yielding d_{smax} = 56.31 mm and ε = 4.28 %. This value was therefore adopted as the calibrated critical Shields parameter for the subsequent temporal scour simulation. The critical Shields parameter was calibrated primarily against the final scour depth, while the temporal scour curves were subsequently examined as a secondary performance check. To further assess the effect of sediment-entrainment threshold on scour development, the predicted temporal scour curves obtained with the three θ_c values are compared with the experimental measurements in Fig. 5.

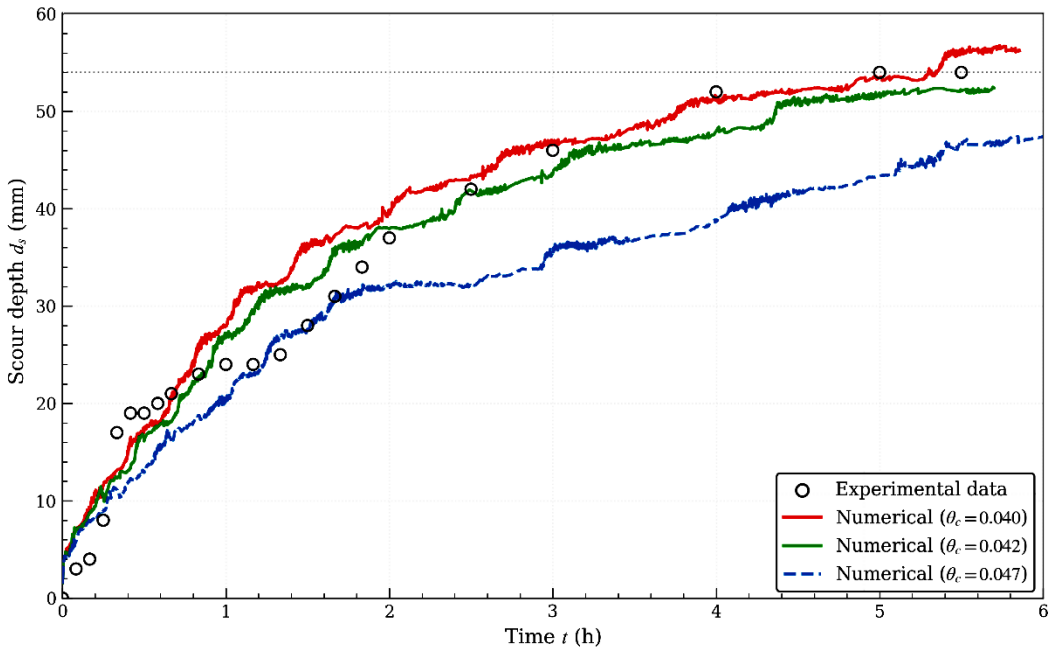


Figure 5. Comparison of temporal scour evolution between experimental measurements and numerical simulations using different critical Shields parameters.

3.3. Temporal scour development and numerical model assessment

The measured and simulated temporal evolution of the maximum local scour depth, $d_s(t)$, over the 330-min clear-water experiment is compared in Fig. 6. The numerical results correspond to the calibrated REEF3D configuration using the medium mesh $\Delta x = 5$ mm and the selected critical Shields parameter, $\theta_c = 0.042$. In the numerical analysis, the maximum scour depth at each time step was determined by scanning the evolving bed surface and identifying the largest local bed lowering within the computational domain. The predicted maximum consistently occurred immediately upstream of the pier, which is also the region where the deepest scour was observed in the physical experiment. Therefore, although the numerical value was not extracted from a prescribed fixed coordinate, the experimental and numerical maximum scour depths correspond to the same physically dominant scour region.

The experimental results show that scour development followed a distinctly non-linear temporal pattern characterized by three stages: rapid initial erosion, transitional scour growth, and a gradual approach toward quasi-equilibrium. During the initial stage, the initially flat sediment bed was subjected to intense localized hydrodynamic forcing around the pier. Within the first 20 min, the measured scour depth increased rapidly to approximately 17 mm, corresponding to about 31% of the final measured scour depth.

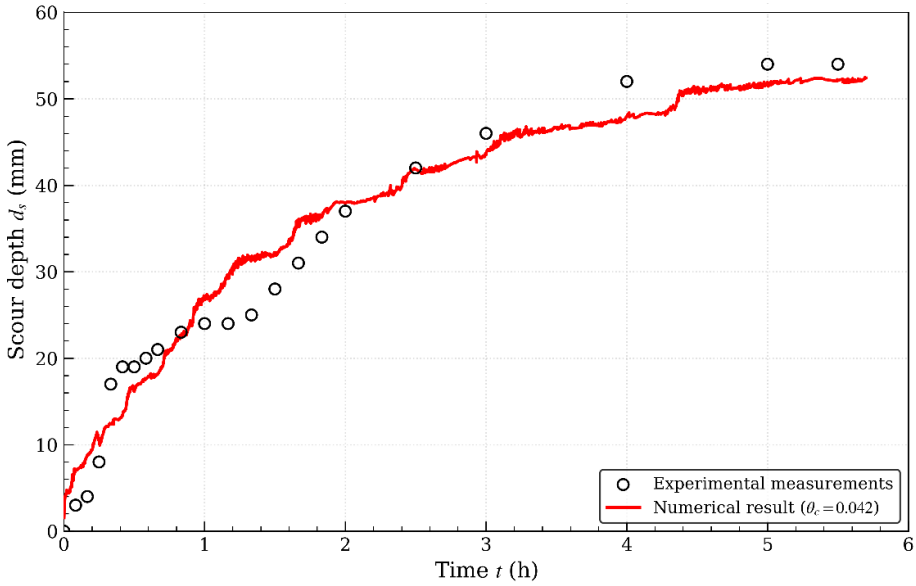


Figure 6. Comparison between measured and simulated temporal evolution of maximum scour depth during the 330-min clear-water experiment using the calibrated REEF3D configuration $\Delta x = 5$ mm, $\theta_c = 0.042$.

The rapid initial scour is consistent with the development of the upstream downflow and horseshoe-vortex system reported by Unger and Hager [30]. At this stage, the relatively undeformed bed provides limited geometric resistance to sediment removal, thereby leading to a high initial scour rate.

Between approximately 20 and 120 min, the scour process entered a transitional stage in which the scour depth continued to increase but at a progressively lower rate. During this period, the measured scour depth increased from approximately 17 to 37 mm. The reduction in scour rate reflects the gradual adjustment of the scour hole, which modifies the near-pier flow field and progressively reduces the efficiency of sediment entrainment.

After approximately 120 min, the scour rate decreased substantially and the measured scour depth gradually approached its final value. The measured maximum scour depth reached approximately 52 mm at 240 min and 54 mm toward the end of the 330-min experiment. The progressively diminishing scour rate is consistent with the characteristic behavior of clear-water local scour, in which the evolving bed morphology weakens the effectiveness of further sediment removal.

The REEF3D simulation reproduced the overall temporal pattern observed experimentally. In particular, the numerical results captured the rapid initial development, the subsequent transitional growth stage, and the gradual stabilization of scour at later times. During the early stage, the model generally predicted somewhat faster scour development than observed in the experiment. This discrepancy may partly result from the immediate development of sediment entrainment in the numerical model, whereas particle mobilization in the physical experiment may be delayed by sediment packing, grain rearrangement, and other small-scale processes not explicitly represented in the model.

During the intermediate stage, the agreement between simulation and experiment improved substantially. The numerical model reproduced the progressive deepening of the scour hole and followed the measured temporal trend reasonably well. This agreement is particularly relevant because it indicates that the coupled hydrodynamic–morphodynamic framework was able to represent the evolution of scour beyond the initial erosion stage.

In the later stage of the process, both experimental and numerical results revealed a decreasing scour rate as the bed profile gradually approached a quasi-equilibrium state. By the end of the run, the simulated maximum scour depth reached 56.31 mm, which compares favorably with the physical measurement of 54.0 mm and indicating close agreement in the final scour magnitude for the calibrated case.

To quantify the temporal prediction accuracy, the mean absolute error (*MAE*) and root mean square error (*RMSE*) were calculated using the 21 experimental measurements. The resulting values were *MAE* = 3.42 mm, *RMSE* = 4.16 mm

These error metrics confirm that the calibrated numerical model reproduced the measured temporal scour development with satisfactory accuracy. More importantly, the comparison shows that REEF3D captured not only the final scour magnitude but also the characteristic evolution of the scour process from rapid initial erosion to gradual stabilization.

Because the mesh resolution and critical Shields parameter were selected using the same experimental dataset, the present results should be interpreted as a calibrated model assessment rather than fully independent validation. The present assessment primarily focuses on the temporal evolution of maximum scour depth. A detailed quantitative assessment of the complete three-dimensional scour-hole geometry and spatial extent is beyond the scope of the present study.

Nevertheless, the agreement in both the temporal trend and final scour magnitude demonstrates the capability of the adopted REEF3D framework to represent the principal characteristics of clear-water local scour development under the investigated conditions.

3.4. Discussion

The results show that the predictive performance of REEF3D is influenced by both numerical resolution and sediment-entrainment parameterization. The mesh-sensitivity analysis indicated that the coarse mesh underestimated the maximum scour depth, whereas the medium

and fine meshes provided much closer predictions. Although the fine mesh gave a slightly smaller error in $d_{s,\max}$, the medium mesh was retained as a practical compromise between predictive accuracy and computational demand.

The critical Shields parameter also had a clear influence on the predicted scour response. Lower values of θ_c increased sediment mobility and produced deeper scour, whereas higher values reduced sediment entrainment and limited scour development. Among the tested values, θ_c = 0.042 provided the closest agreement with the measured maximum scour depth and was therefore adopted for the calibrated simulation.

The temporal comparison further demonstrated that the calibrated model reproduced the main characteristics of clear-water scour development, including rapid initial erosion, transitional growth, and gradual stabilization. The remaining discrepancies during the early stage are likely associated with idealized numerical representation of sediment mobilization and near-bed processes that are difficult to reproduce explicitly in a continuum morphodynamic model. Nevertheless, the low *MAE* and *RMSE* values indicate satisfactory agreement over the full test duration.

These findings indicate that final scour depth alone is insufficient for assessing morphodynamic model performance. A parameter set may reproduce the final scour magnitude while still exhibiting noticeable discrepancies in the early-stage scour rate. For temporal scour applications, both final-depth agreement and transient development should therefore be examined.

Extension of the present numerical framework to prototype-scale bridge piers requires preservation of the dominant dimensionless hydraulic and sediment-transport parameters rather than direct geometric scaling of the present configuration. Relevant similitude parameters include the Froude number for free-surface flow, (U/U_c) for sediment mobility, relative flow depth (y/D), relative sediment size (d_{50}/D), and Shields-type mobility parameters. At prototype scale, Reynolds-number effects should also be checked to ensure that the flow remains within an appropriate fully turbulent regime. Consequently, the calibrated mesh resolution and critical Shields parameter obtained in the present laboratory-scale case should not be transferred directly to prototype applications without additional scale assessment and validation.

The present assessment should therefore be interpreted as case-specific. Both the mesh resolution and the critical Shields parameter were selected using the same experimental dataset, meaning that the results represent calibration rather than fully independent validation. In addition, only one cylindrical-pier geometry, one uniform sediment condition, and one steady clear-water flow condition were investigated. Further studies covering broader hydraulic intensities, sediment sizes, and pier configurations are required to evaluate the general applicability of the numerical framework.

4. CONCLUSIONS

This study investigated clear-water local scour around a cylindrical bridge pier using laboratory measurements and three-dimensional morphodynamic simulation with REEF3D. The main conclusions are as follows.

1. The experimental scour process exhibited three characteristic stages: rapid initial erosion, transitional scour growth, and gradual approach toward quasi-equilibrium. The measured maximum scour depth reached approximately 54 mm during the 330-min test.

2. Mesh resolution significantly influenced the predicted maximum scour depth. The medium mesh with Δx = 5 mm achieved accuracy comparable to the fine mesh with substantially fewer computational cells and was therefore adopted for the subsequent simulations.
3. The critical Shields parameter strongly affected sediment entrainment and scour prediction. Among the tested values, θ_c = 0.042 gave the closest agreement with the measured scour depth and was adopted as the calibrated value.
4. Using the selected mesh and θ_c, REEF3D reproduced the overall temporal scour development with satisfactory accuracy. The comparison with 21 experimental measurements yielded (*MAE*=3.42) mm and (*RMSE*=4.16) mm, indicating that the model captured both the magnitude and progression of scour reasonably well.

The results are specific to the investigated cylindrical pier, uniform sediment, and steady clear-water condition. Because the numerical parameters were calibrated using the same experimental dataset, further independent validation under broader hydraulic, sediment, and pier conditions is required before general engineering application.

ACKNOWLEDGMENT

This research is funded by University of Transport and Communications (UTC) under grant number T2026-CT-012.

REFERENCES

[1]. L. Deng, W. Wang, Y. Yu, State-of-the-art review on the causes and mechanisms of bridge collapse, Journal of Performance of Constructed Facilities, 30 (2016) 04015005. https://doi.org/10.1061/(ASCE)CF.1943-5509.0000731

[2]. W. Xiong, C. S. Cai, R. Zhang, H. Shi, C. Xu, Review of hydraulic bridge failures: Historical statistic analysis, failure modes, and prediction methods, Journal of Bridge Engineering, 28 (2023). https://doi.org/10.1061/JBENF2.BEENG-5763

[3]. L. Deng, C. S. Cai, Bridge scour: Prediction, modeling, monitoring, and countermeasures-Review, Practice Periodical on Structural Design and Construction, 15 (2010). https://doi.org/10.1061/(ASCE)SC.1943-5576.0000041

[4]. H. Q. Mai, P. D. Nguyen, A review on protection methods against debris accumulation for bridge in mountain areas, in: C. Ha-Minh, D. Dao, F. Benboudjema, S. Derrible, D. Huynh, A. Tang (Eds.), CIGOS 2019, Innovation for Sustainable Infrastructure, Lecture Notes in Civil Engineering, vol. 54, Springer, Singapore, 2020, pp. 233-238. https://doi.org/10.1007/978-981-15-0802-8_34

[5]. G. Zhang, Y. Liu, J. Liu, S. Lan, J. Yang, Causes and statistical characteristics of bridge failures: A review, Journal of Traffic and Transportation Engineering (English Edition), 9 (2022) 388-406. https://doi.org/10.1016/j.jtte.2021.12.003

[6]. B. W. Melville, S. E. Coleman, Bridge Scour, Water Resources Publications, Highlands Ranch, Colorado, 2000.

[7]. J. E. Richardson, V. G. Panchang, Three-dimensional simulation of scour-inducing flow at bridge piers, Journal of Hydraulic Engineering, 124 (1998) 530-540. https://doi.org/10.1061/(ASCE)0733-9429(1998)124:5(530)

[8]. H. N. C. Breusers, G. Nicollet, H. W. Shen, Local scour around cylindrical piers, Journal of Hydraulic Research, 15 (1977) 211-252. https://doi.org/10.1080/00221687709499645

[9]. D. C. Froehlich, Analysis of onsite measurements of scour at piers, in: Hydraulic Engineering: Proceedings of the 1988 National Conference on Hydraulic Engineering, ASCE, Colorado Springs, CO, 1988, pp. 534-539.

[10]. E. V. Richardson, S. R. Davis, Evaluating Scour at Bridges, fourth ed., Hydraulic Engineering Circular No. 18, FHWA-NHI-01-001, Federal Highway Administration, 2001.

[11]. T. T. Pham, Q. H. Mai, Evaluating bridge abutment scour models under varying contraction, Roads and Bridges – Drogi i Mosty, 25 (2026) 155-166. https://doi.org/10.7409/rabdim.026.011

[12]. S. Dey, S. Z. Ali, The universal two-fifths law of pier scour, Physics of Fluids, 36 (2024) 041401. https://doi.org/10.1063/5.0200865

[13]. A. Khosronejad, S. Kang, F. Sotiropoulos, Experimental and computational investigation of local scour around bridge piers, Advances in Water Resources, 37 (2012) 73-85. https://doi.org/10.1016/j.advwatres.2011.09.013

[14]. W. Xiong, C. S. Cai, B. Kong, X. Kong, CFD simulations and analyses for bridge-scour development using a dynamic-mesh updating technique, Journal of Computing in Civil Engineering, 30 (2016). https://doi.org/10.1061/(ASCE)CP.1943-5487.0000458

[15]. W. Xiong, P. Tang, B. Kong, C. S. Cai, Computational simulation of live-bed bridge scour considering suspended sediment loads, Journal of Computing in Civil Engineering, 31 (2017). https://doi.org/10.1061/(ASCE)CP.1943-5487.0000689

[16]. A. M. Bento, J. P. Pêgo, T. Viseu, L. Couto, Scour development around an oblong bridge pier: A numerical and experimental study, Water, 15 (2023) 2867. https://doi.org/10.3390/w15162867

[17]. W. Huang, Q. Yang, H. Xiao, CFD modeling of scale effects on turbulence flow and scour around bridge piers, Computers & Fluids, 38 (2009) 1050-1058. https://doi.org/10.1016/j.compfluid.2008.01.029

[18]. P. Yu, L. Zhu, Numerical simulation of local scour around bridge piers using novel inlet turbulent boundary conditions, Ocean Engineering, 218 (2020) 108166. https://doi.org/10.1016/j.oceaneng.2020.108166

[19]. P. Yu, S. Xu, J. Chen, L. Zhu, J. Zhou, L. Yu, Z. Sun, Three-dimensional numerical modeling of local scour around bridge foundations based on an improved wall shear stress model, Journal of Marine Science and Engineering, 12 (2024) 2187. https://doi.org/10.3390/jmse12122187

[20]. M. Hamidi, M. Sadeqlu, A. Mahdian Khalili, Investigating the design and arrangement of dual submerged vanes as mitigation countermeasure of bridge pier scour depth using a numerical approach, Ocean Engineering, 299 (2024) 117270. https://doi.org/10.1016/j.oceaneng.2024.117270

[21]. H. Bihs, A. Kamath, M. Alagan Chella, A. Aggarwal, Ø. A. Arntsen, A new level set numerical wave tank with improved density interpolation for complex wave hydrodynamics, Computers & Fluids, 140 (2016) 191-208. https://doi.org/10.1016/j.compfluid.2016.09.012

[22]. REEF3D, REEF3D User Guide. https://github.com/REEF3D/REEF3D/blob/master/REEF3D-UserGuide.pdf.

[23]. M. S. Afzal, H. Bihs, A. Kamath, Ø. A. Arntsen, Three-dimensional numerical modeling of pier scour under current and waves using level-set method, Journal of Offshore Mechanics and Arctic Engineering, 137 (2015) 032001. https://doi.org/10.1115/1.4029999

[24]. G. Fleit, S. Baranya, R. Ehlers, H. Bihs, CFD modeling of flow and local scour around submerged bridge decks, Journal of Coastal and Hydraulic Structures, 3 (2023) 26. https://doi.org/10.48438/jchs.2023.0026

[25]. D. P. Nguyen, Local scour at bridge piers under clear-water conditions, 2013 (in Vietnamese). https://giaothong.tapchixaydung.vn/xoi-cuc-bo-tru-cau-trong-dieu-kien-xoi-nuoc-trong-1834347.htm.

[26]. B. Liang, S. Du, X. Pan, L. Zhang, Local scour for vertical piles in steady currents: Review of mechanisms, influencing factors and empirical equations, Journal of Marine Science and Engineering, 8 (2020) 4. https://doi.org/10.3390/jmse8010004

[27]. D. C. Wilcox, Simulation of transition with a two-equation turbulence model, AIAA Journal, 32 (1994) 247-255. https://doi.org/10.2514/3.59994

[28]. F. Engelund, J. Fredsøe, A sediment transport model for straight alluvial channels, Hydrological Research, 7 (1976) 293-306. https://doi.org/10.2166/nh.1976.0019

[29]. S. Dey, Fluvial Hydrodynamics: Hydrodynamic and Sediment Transport Phenomena, revised second ed., Springer, Cham, Switzerland, 2024. https://doi.org/10.1007/978-3-031-26038-4

[30]. J. Unger, W. H. Hager, Down-flow and horseshoe vortex characteristics of sediment embedded bridge piers, Experiments in Fluids, 42 (2007) 1-19. https://doi.org/10.1007/s00348-006-0209-7